JGR Space Physics

RESEARCH ARTICLE
10.1029/2020JA028119

Observational Evidence for the Role of Hall Conductance in Alfvén Wave Reflection

Magnus F. Ivarsen[1], Jaeheung Park[2,3], Young-Sil Kwak[2,3], Yaqi Jin[1], David J. Knudsen[4], and Lasse B. N. Clausen[1]

[1]Department of Physics, University of Oslo, Oslo, Norway, [2]Korea Astronomy and Space Science Institute, Daejeon, South Korea, [3]Department of Astronomy and Space Science, Korea University of Science and Technology, Daejeon, South Korea, [4]Department of Physics and Astronomy, University of Calgary, Calgary, Alberta, Canada

Key Points:
- Enhanced Hall conductance plays a major role in driving Alfvén wave reflection, especially on the nightside ionosphere
- High-energy precipitation provided by the nightside aurora provides an explanation for the enhanced Hall conductance
- Pedersen conductance and solar zenith angle are strong indicators for Alfvén wave reflection on the dayside ionosphere

Correspondence to:
M. F. Ivarsen,
m.f.ivarsen@fys.uio.no

Citation:
Ivarsen, M. F., Park, J., Kwak, Y.-S., Jin, Y., Knudsen, D. J., & Clausen, L. B. N. (2020). Observational evidence for the role of Hall conductance in Alfvén wave reflection. *Journal of Geophysical Research: Space Physics*, *125*, e2020JA028119. https://doi.org/10.1029/2020JA028119

Received 15 APR 2020
Accepted 2 NOV 2020
Accepted article online 21 NOV 2020

Abstract Electromagnetic energy carried by magnetohydrodynamic modes is an important mechanism in the energy transfer between the magnetosphere and the ionosphere. Alfvén waves are known to carry field-aligned currents and thus play an important role in the dynamics of the ionosphere-magnetosphere coupling. The role of Hall conductance in this interplay has been explored in magnetohydrodynamic models of the ionosphere but has hitherto not been observed in situ. We use 5 years of observations from the Swarm mission to shed light on this interplay. We present a high-latitude climatology of both the measured Poynting flux and the measured Alfvén wave reflection coefficient. Our results indicate that high-energy precipitation, which penetrates deep into the ionosphere and directly leads to strongly enhanced Hall conductance, is an important cause of positively interfering Alfvén wave reflection. We present such observational evidence and, with that, suggest that Hall conductance is substantially more important in the ionospheric wave reflection climatology than hitherto believed.

1. Introduction

Of particular importance for the high-latitude ionosphere is the large-scale field-aligned current (FAC) system, also called the Birkeland current system (Cowley, 2000; Iijima & Potemra, 1978). Through the large-scale currents flowing in and out of the ionosphere, a massive transfer of energy from the magnetosphere and the solar wind to the ionosphere occurs (Cowley, 2000; Cowley & Lockwood, 1992; Dungey, 1961; Siscoe & Huang, 1985). The FAC flows, as the name suggests, along magnetic field lines, which in the polar regions are almost normal to Earth's surface. Electrically, the conductance needed to support the FACs is provided by the magnetic field-perpendicular Pedersen conductance, while, conversely, the conductance perpendicular to both the magnetic and electric field is called Hall conductance.

In the ionosphere, changes in Pedersen conductance are broadly predicted by changes in solar extreme-ultraviolet (EUV) photoionization, and so solar zenith angle (SZA, the angle between a vector normal to Earth's surface and the Sun), is a strong predictor for Pedersen conductance (Brekke & Moen, 1993; Fujii et al., 1981; Ridley et al., 2004; Vickrey et al., 1981). This EUV reliance, which translates to a reliance on SZA, creates a clear seasonal dependency in the FAC system, with stronger Pedersen conductance and stronger FAC amplitudes during local summer—when the polar regions experience perpetual sunlight—compared to local winter (Coxon et al., 2016; Haraguchi et al., 2004; Yamamoto et al., 2003).

In addition to EUV photoionization, both Pedersen and Hall conductivities also receive contributions from precipitating electrons (Vickrey et al., 1981). However, in the *E* region ionosphere, Hall conductivity peaks at a lower altitude than Pedersen conductivity, making Hall conductance more susceptible to deeply penetrating precipitating electrons and thus to higher energy electrons (Coumans et al., 2004; Nishimura et al., 2020). In fact, when considering high-latitude Hall conductance, auroral precipitation has a greater impact than EUV photoionization (Lotko et al., 2014). Using incoherent scatter radar measurements during nightside pulsating aurora, Hosokawa et al. (2010) found that Hall conductance doubled during periods of elevated auroral activity, at times reaching 30 S, and was up to 3 times greater than the measured Pedersen conductance. Similar results were reported by Senior et al. (1982), likewise showing a Hall to Pedersen conductance ratio of 3 in incoherent scatter radar measurements under similar conditions. Since the flux of highly energetic auroral precipitation exhibits opposite seasonal behavior to that of EUV photoionization

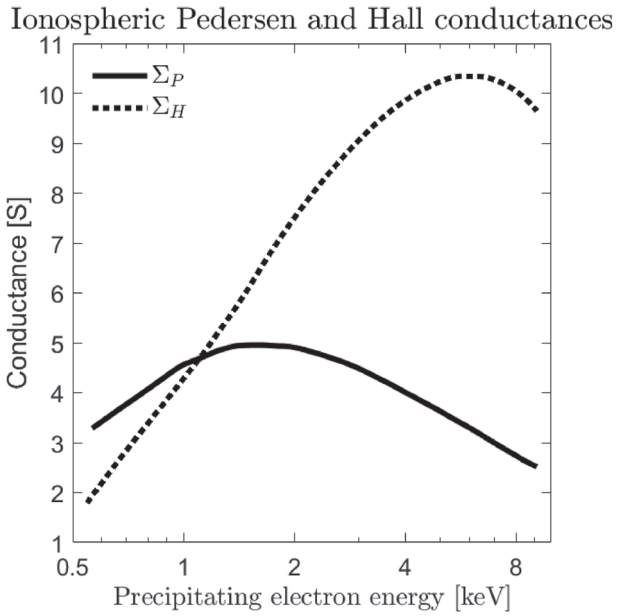

Figure 1. The impact of electron precipitation on ionospheric Pedersen (solid line) and Hall (dotted line) conductances, with precipitating electron energy shown on a logarithmic scale along the *x* axis. While the impact on Pedersen conductance peaks at an electron energy around 1.5 keV, the lower-altitude Hall conductance receives a peak impact from electron precipitation at an energy around 6 keV. The figure is plotted using values provided in Vickrey et al. (1981) (see also Coumans et al., 2004).

(Newell et al., 2010), Hall conductance does not exhibit the same seasonal dependencies as Pedersen conductance (Kwak & Richmond, 2007). In Figure 1, we show the impact of deeply penetrating electron precipitation on Pedersen and Hall conductances, where we use values given in Vickrey et al. (1981). One can see that, while Pedersen conductance is more strongly impacted by low-energy precipitation, Hall conductance can get a many times higher contribution for high-energy electrons.

The diffuse aurora is a frequent source of high-energy precipitating electron and is the dominant source of total auroral energy flux (Newell et al., 2009; Nishimura et al., 2020). Consisting of higher energy particles than its counterpart, the discrete aurora, the diffuse aurora is largely observed in the equatorward portion of the auroral oval (Nishimura et al., 2020). The nightside diffuse aurora is strongest in the early morning sector, with the region of strongest energy flux centered on 3 h magnetic local time (MLT) (Newell et al., 2010). Nightside pulsating aurora, a type of diffuse aurora, occurs almost daily in the Northern Hemisphere between midnight and 07 h MLT, largely between 63° and 73° magnetic latitudes (Grono & Donovan, 2020). Conversely, dayside diffuse aurora occurs further poleward, near cusp latitudes, and tends to be associated with substorms (Han et al., 2015; Nishimura et al., 2020). The dayside diffuse aurora tends to have a stronger number flux rather than to carry high-energy electrons (Newell et al., 2010).

As mentioned, seasonal changes in the energy of auroral precipitation are opposite from those of EUV photoionization: Precipitating particle energy is markedly higher during local winter compared to local summer (Liou et al., 2001). Overall, the number flux of precipitating electrons tends to be higher during local summer and on the dayside, while, conversely, the average energy of precipitating electrons tends to be higher during local winter and even in darkness (Liou et al., 2001). Returning to diffuse aurora, a local winter increase in precipitating electron energy causes the total energy flux of diffuse aurora to peak during local winter (Newell et al., 2010; Nishimura et al., 2020). As mentioned, compared to Pedersen conductance, changes in Hall conductance are more dependent on high-energy deeply penetrating precipitation; we thus expect Hall conductance to get a peak contribution from precipitation during local winter and in darkness (SZA > 90°).

When trapped in resonators and waveguides, magnetohydrodynamic (MHD) modes in the ionosphere deposit electromagnetic energy (Fedorov et al., 2016). Of these MHD modes, Alfvén waves (Alfvén, 1942) are the only waves associated with FACs (Burke et al., 2016; Siscoe, 1983; Yoshikawa & Itonaga, 1996). The dynamics of Alfvén waves can be affected by the ionospheric Alfvén resonator (IAR), which is an effective cavity created by the altitude gradient in the Alfvén velocity, which causes modulation of the dynamics surrounding wave reflection (Lysak, 1991). The reflection coefficient can be expressed in the following manner (Park et al., 2017):

$$\alpha_0 = \frac{\Sigma_P - \Sigma_A}{\Sigma_P + \Sigma_A}, \tag{1}$$

where $\Sigma_{P,A}$ are the Pedersen and Alfvén conductances respectively. Note that the sign convention in Equation 1 is opposite from that used in, for example, Lysak (1991) and therefore can be viewed as a magnetic, as opposed to electric, field reflection coefficient.

Equation 1 offers key insight into the dynamics surrounding wave reflection. If Pedersen and Alfvén conductances are equal, $\alpha_0 = 0$, and there is no wave reflection. If, on the other hand, $\alpha_0 \neq 0$, the incoming wave is reflected, leading to an outgoing wave. The sign of α_0 controls the sign of the outgoing wave magnetic field component, meaning that the sign of α_0 controls whether there is positive or negative interference between the incoming and outgoing wave (Lysak, 1991). The two extremes, $\alpha_0 = \pm 1$, correspond to perfect constructive interference and cancelation of the *B* field, respectively (Burke et al., 2016; Fedorov et al., 2016; Park et al., 2017). That is, $\alpha_0 = +1$ corresponds to the reflected *E* field being antiparallel to the incident *E*

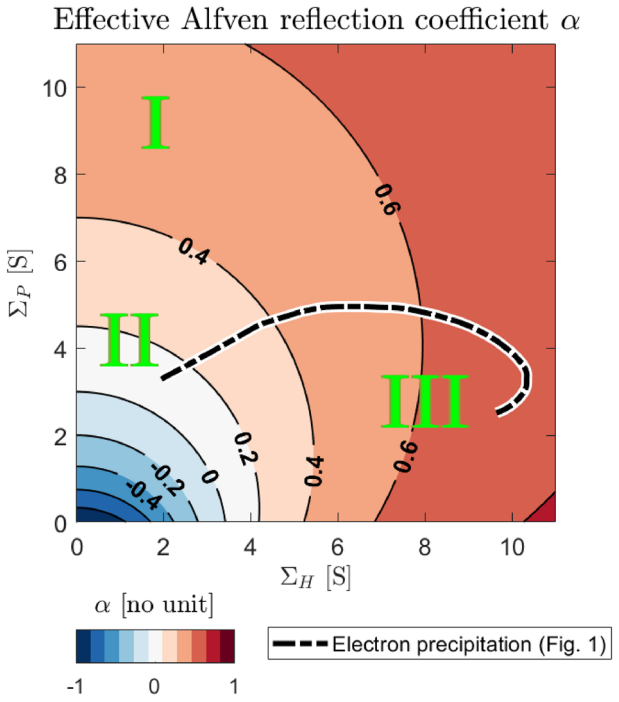

Figure 2. Contour lines of constant α (Equation 2) plotted against Pedersen conductance on the *y* axis, and Hall conductance on the *x* axis, with a constant Alfvén conductance $\Sigma_A = 3$ S. The dot-dashed black line shows the particular ratio of Σ_H to Σ_P displayed in Figure 1. For input values in Equation 2, we used Equations 58–61 in Yoshikawa and Itonaga (2000) for η and Equation 1 in the present study for values of α_0. The values of α for $\Sigma_H = 0$ (close to the *y* axis) correspond to α_0 (Equation 1). Three regimes are marked in green roman numerals: high Σ_P-low Σ_H (I), intermediate Σ_P-intermediate Σ_H (II), and low Σ_P-high Σ_H (III), to be referenced in the text.

field, with equal magnitude. This yields zero net *E* field and a perfect constructive interference in the net *B* field. Conversely, $\alpha_0 = -1$ here corresponds to the net *E* field undergoing perfect constructive interference, with zero net *B* field.

Since Σ_A is independent of Hall conductance, for a given value of Σ_A, α_0 in Equation 1 should depend only on Pedersen conductance, and thus on SZA. In reality, however, the Alfvén wave reflection coefficient is also affected by Hall conductance (Fedorov et al., 2018; Waters et al., 2013; Yoshikawa & Itonaga, 2000). Yoshikawa and Itonaga (2000), developing a model of the reflection and mode conversion of MHD waves in the high-latitude ionosphere, found that the role of the Hall conductance is to couple energy from the shear Alfvén mode to the compressional mode, which is generally evanescent within the auroral zone. Since the compressional mode is not guided by the magnetic field, it can radiate horizontally away from the coupling region and couple to more distant ionospheric regions. Furthermore, Yoshikawa and Itonaga (2000) found that the following expression is consistent with the theoretical underpinnings of MHD,

$$\alpha = \alpha_0 + (\alpha_0 - 1)\frac{\eta}{1-\eta}, \tag{2}$$

where α is the effective Alfvén reflection coefficient, and η is the mutual inductance coefficient. In broad terms, η is determined mostly by $(\Sigma_H/\Sigma_P)^2$, Σ_H being Hall conductance, and incorporates all the contributions to wave reflection by the Hall conductance (Yoshikawa & Itonaga, 2000). Again, $\alpha = +1$ corresponds to perfect constructive interference of the magnetic component of the wave, which yields zero net *E* field and a perfect constructive interference in the net *B* field, while $\alpha = -1$ corresponds to the net *E* field undergoing perfect constructive interference, with zero net *B* field.

The effect of Hall conductance on α is illustrated in Figure 2, where we show contour lines of constant α plotted against Pedersen conductance on the *y* axis, and Hall conductance on the *x* axis, with an Alfvén conductance $\Sigma_A = 3$ S. The values of α for $\Sigma_H = 0$ (close to the graph's *y* axis) correspond to an unmodified reflection coefficient, α_0 (Equation 1). In addition we display, in dot-dashed black line, the particular ratio of Σ_H/Σ_P shown in Figure 1, illustrating the impact of precipitation on α, for energies of precipitating electrons ranging from 0.5 to 8 keV. If moving one's finger along Figure 2 from left to right, one would cross several more contour lines on the *bottom* of the graph than one would on the top. In other words, an increase in Hall conductance has a much greater impact on α when the Pedersen conductance is low. This is true also for moderate ratios of $\Sigma_H/\Sigma_P \approx 2$. Such conditions are fulfilled for high SZA, for example, during local winter or on the nightside ionosphere, where a precipitation-induced increase in Hall conductance would subsequently lead to an increase in the Alfvén reflection coefficient. In fact, high-energy deep-penetrating electron precipitation can cause observed Hall conductance to be up to 5 times greater than Pedersen conductance (Coumans et al., 2004; Vickrey et al., 1981), creating conditions for the effect shown in Figure 2 to manifest. Note that the values of α displayed in Figure 2 are not meant to form a prediction but are meant as an example of how α is impacted by Hall conductance under example conditions.

The purpose of the present study is to investigate the relationship between precipitation-induced Hall conductance and Alfvén wave reflection. This relationship has been pointed out by several theoreticians (see, e.g., Fedorov et al., 2018; Waters et al., 2013; Yoshikawa & Itonaga, 2000) but has hitherto not been observed. To accomplish this, we use a large data set of in situ observations from the Swarm mission to estimate ionosphere Alfvén reflection coefficients and perform a statistical analysis on the outcome.

2. Methodology

In this study we use data from Swarm A, one of three satellites in the Swarm mission (Friis-Christensen et al., 2006; Knudsen et al., 2017). Swarm A orbits Earth at an altitude of 460 km in the *F* region ionosphere,

carrying a host of scientific instruments. In this study, we use electric field data from the Thermal Ion Imager (TII) 2 Hz ion drift data set (Knudsen et al., 2017; Lomidze et al., 2019). Along- and cross-satellite track components of the electric field are estimated based on the TII image moments, where the E field reflects the impact of ionospheric flow. The data product provides the 2 Hz E field, in addition to 50 Hz B field data from the onboard Vector Field Magnetometer, downsampled to 2 Hz. Both the E and B field data are provided in satellite track coordinates. In broad outlines, we follow Park et al. (2017) in transforming the E and B fields to the mean-field-aligned (MFA) coordinate system. The procedure is as follows. First, we apply a second-order Savitzky-Golay filter with a window size of 225 s to the magnetic field data to obtain the ambient magnetic field. Due to inaccuracies in the filtering near the geographic poles, we exclude points sampled below −78° magnetic latitude (MLAT) and above 82° MLAT, limits determined after extensive testing. The residual 2 Hz B field is then obtained after subtracting the mean field. The next step is to transform the residual B field and the E field vectors into the MFA coordinate system, after we apply a high-pass filter to the E field data to remove large-scale offsets. The MFA coordinate system has one component parallel to the mean field (z), one pointing in geomagnetic east (y), with the third component completing the triad (meridional, x).

Again following Park et al. (2017) and Burke et al. (2016), we can now calculate quantities related to ionospheric Alfvén wave reflection. The Alfvén wave reflection coefficient (Equation 2) is approximated by

$$\alpha_{obs} = \frac{K - |S_z|}{K + |S_z|}, \tag{3}$$

where K is defined as

$$K = \frac{V_A}{\mu_0}(B_x^2 + B_y^2), \tag{4}$$

while S_z is the field-parallel Poynting flux,

$$S_z = \frac{E_x B_y - E_y B_x}{\mu_0}, \tag{5}$$

where $B_{x,y}$ is the 2 Hz residual B field, and $E_{x,y}$ is the residual E field, x and y refer to MFA meridional and MFA east coordinates, respectively; μ_0 is the vacuum permeability, and V_A is the Alfvén speed. S_z represents the flux of electromagnetic energy along the field lines and is a measure of energy transfer between the magnetosphere and the ionosphere (Gary et al., 1995; Waters et al., 2004). Note that, as a consequence of the model developed by Yoshikawa and Itonaga (2000), we expect Equation 3 to measure the effective Alfvén wave reflection coefficient, which will approach the theoretical value (Equation 1) only when the impact of Hall conductance is negligible.

Before evaluating Equation 3, we follow Park et al. (2017) in imposing a series of data selection criteria to ensure good data quality: The magnitude of the Poynting flux should be at least 1 μW/m^2, and the angle between the E and B fields should not be smaller than 78°. Additionally, the transverse components of the B and E fields should correlate reasonably well. Specifically, in a 6 s window centered on the relevant data point, *either* B_y and E_x *or* B_x and E_y should have an absolute Pearson correlation coefficient (the degree to which points fall on a straight line when plotted against each other) of at least 0.4 (Park et al., 2017). We will refer to this quantity, calculated for every 6 s bin, as the E-B correlation, or ρ_{EB}. Given that the criteria are fulfilled, we calculate the median α_{obs}, ρ_{EB} and the SZA for every 6 s data bin mentioned above. The SZA is adjusted for the altitude of Swarm A orbit, meaning that the sunlight terminator at an altitude of 460 km is defined as 90° SZA.

In Figure 3 we illustrate the process. In Panel (a), we present a stretch of the orbit of Swarm A, showing the satellite approaching the Southern Hemisphere nightside aurora from the dayside. For a 4 min stretch centered on 13:52:00 UT, we show the 2 Hz residual magnetic field (Panel b) and the electric field (Panel c). In Panel (d), we show the Poynting flux parallel to the mean field (Equation 5), and in Panel (e) we show the resulting 6 s median α_{obs} (Equation 3), along with ρ_{EB}, the maximum E-B Pearson correlation coefficient for the 6 s windows. We see that as Swarm A approaches the Southern Hemisphere pre-midnight aurora, the observed Alfvén reflection coefficient α_{obs} (Equation 3) fluctuates around 0, before increasing to 1 at 13:51:00 UT, dipping to 0 at 13:51:30 UT, then hovering around 1 until 13:53:15 UT. The observed Poynting flux S_z (Equation 5) indicates strong electromagnetic flux roughly between 13:51:15 UT and 13:52:50 UT, which can indicate the presence of Alfvén waves (Keiling et al., 2003). The upward flowing Poynting flux

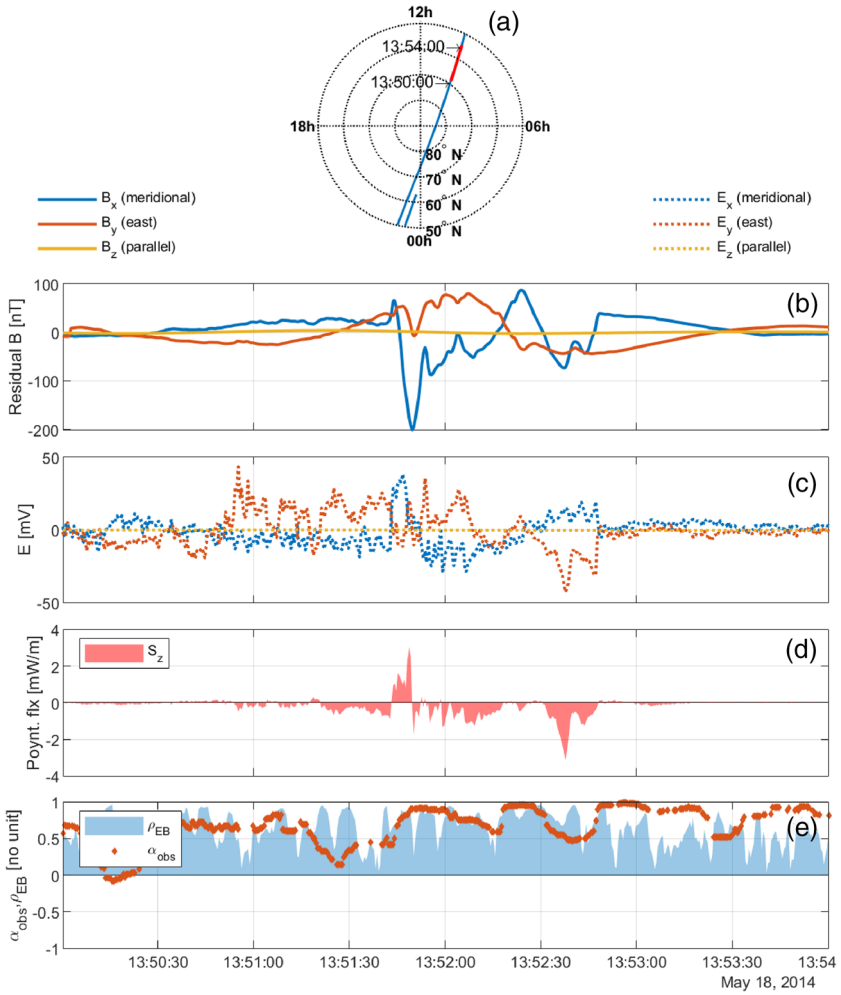

Figure 3. (a) The orbit of Swarm A across the Northern Hemisphere polar cap during an extended time period centered on 18 May 2014 at 13:52:00 UT. The 2 Hz residual magnetic field (b), and the electric field (c), both in MFA coordinates, for a 4 min time period centered on 13:52:00 UT. (d) The Poynting flux S_z (Equation 5). Positive values of S_z correspond to flux flowing parallel to the mean field, which in the Southern Hemisphere becomes upward going flux. (e) The resulting 6 s median α_{obs} (Equation 3), along with ρ_{EB}, the maximum correlation between either B_x and E_y or B_y and E_x. All times displayed in the figure are in UT.

at 13:51:50 UT is incidentally accompanied by $\alpha_{obs} \sim 1$, and a strong increase in the magntitude of B_x, the meridional component of the magnetic perturbations. Note that, as Figure 3 shows data from the Southern Hemisphere, negative values of S_z correspond to downward going flux. Throughout the time period, ρ_{EB} generally stays above the threshold of 0.4, with interspersed dips occurring.

As a commentary on the limitations of the methodology used in the present study, note that we are not able to infer the frequency of Alfvén waves based on Swarm A data and that we are rather able to calculate the nature of any Alfvén wave reflection events that could occur, events that would take place in a reflection layer below the satellite altitude (Pakhotin et al., 2018). Any signature of Alfvén waves at the location of Swarm A is encountered by the satellite as quasi-stationary FAC structures. The distance between the satellite and the reflection layer is assumed to be small compared to the field-aligned wavelength of the Alfvén waves whose signatures might be present at the satellite altitude (Knudsen, 1990). As such, we cannot pinpoint the Alfvén wave frequency associated with any reflection event.

3. Results

We aggregate Swarm A TII data according to the selection criteria detailed above, gathered between ±60° and ±86° MLAT. The data cover a period from 18 January 2014 until 3 March 2019, with uneven breaks in

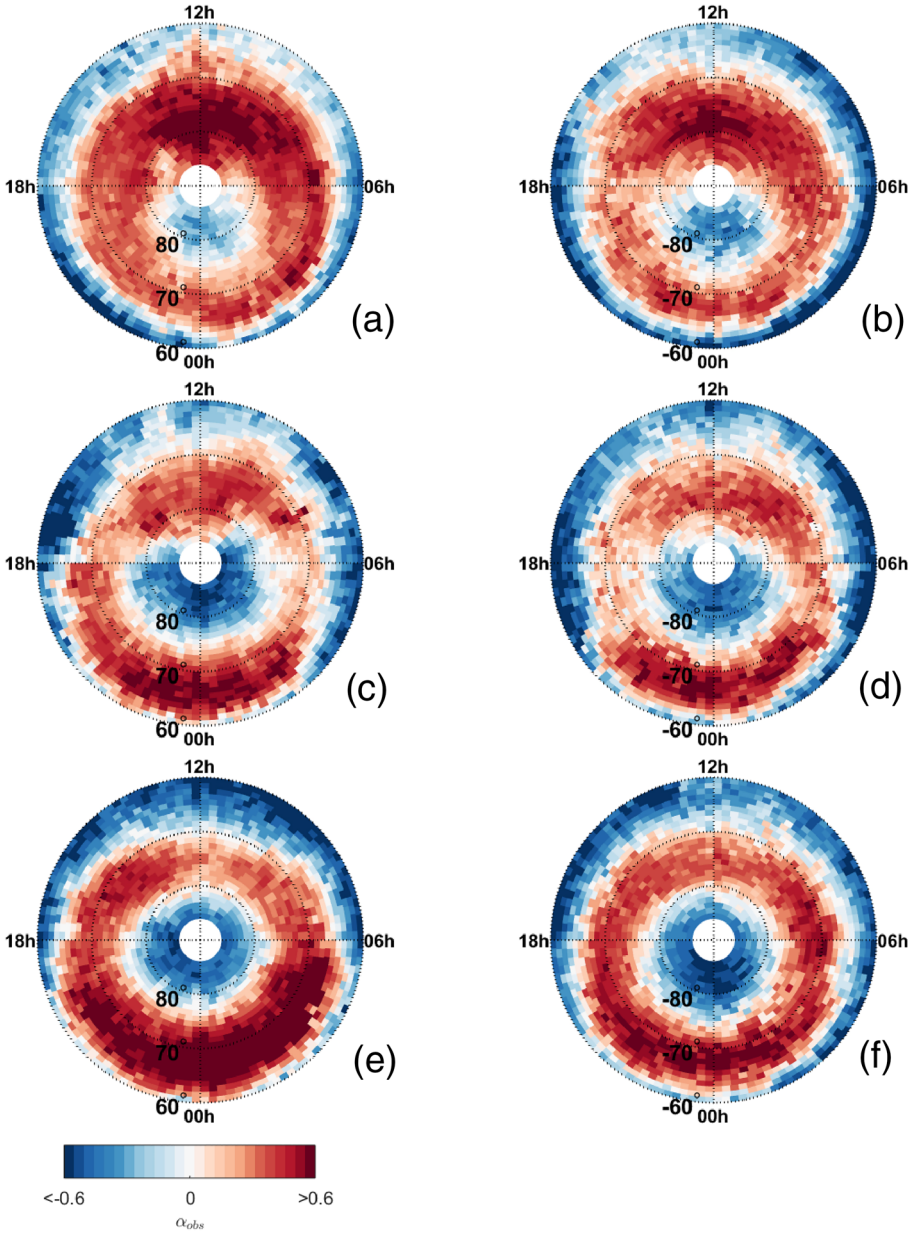

Figure 4. Climatological maps of the high-latitude ionosphere showing the distribution of observed α_{obs} between ±60° and ±86° MLAT, where MLT is marked on each graph; 12 h (noon) faces the Sun. (a, c, and e) The Northern Hemisphere summer, equinoxes, and winter, respectively; (b, d, and f) the same local seasons for the Southern Hemisphere. Summer and winter are here defined as a 131 day period centered on each solstice, while the combined equinoxes consist of a 65.5 day period centered on both the autumn and spring equinoxes, meaning each season spans the same number of days each year, with overlap. The data used comes from Swarm A and spans a time period from 18 January 2014 until 3 March 2019.

the data coverage; however, all seasons are represented with roughly the same number of data points. From the data, a total number of 16 million 6 s segments of Swarm A data made the selection according to the criteria outlined above. In Figure 4, we show the distribution of Alfvén reflection coefficient, α_{obs}, during local summer, equinoxes, and winter in climatological maps of the ionosphere. In each panel, an MLT of 12 h is situated on the top of each graph. Here, local summer and winter are defined as a 131 day period centered on each solstice, while the combined equinoxes consist of a 65.5 day period centered on both the autumn and spring equinoxes, such that each season spans the same number of days each year, with overlap. The Swarm satellites span all MLTs in a time period of 131 days, meaning each season contains data from

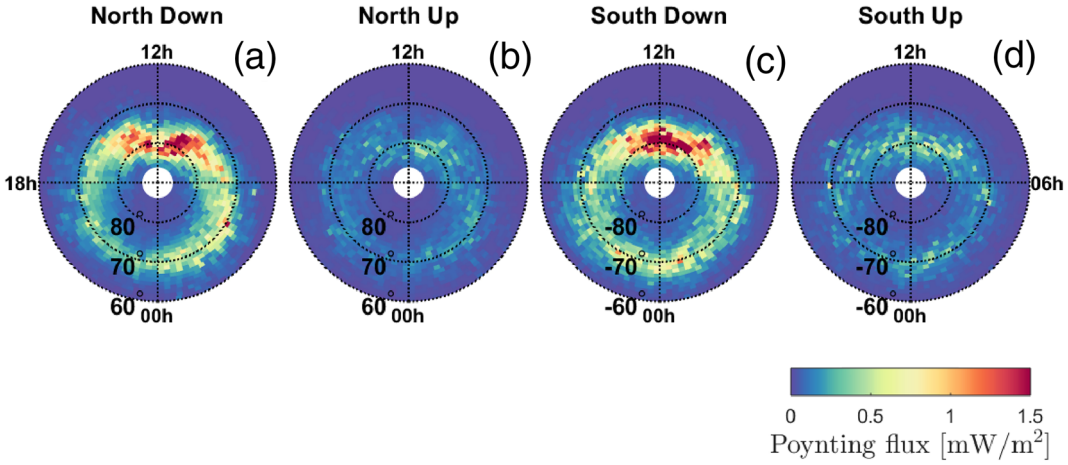

Figure 5. Climatological distribution of the Poynting flux, for the downward going (a, c) and upward going (b, d) Poynting vector. (a and b) The Northern Hemisphere; (c and d) the Southern Hemisphere.

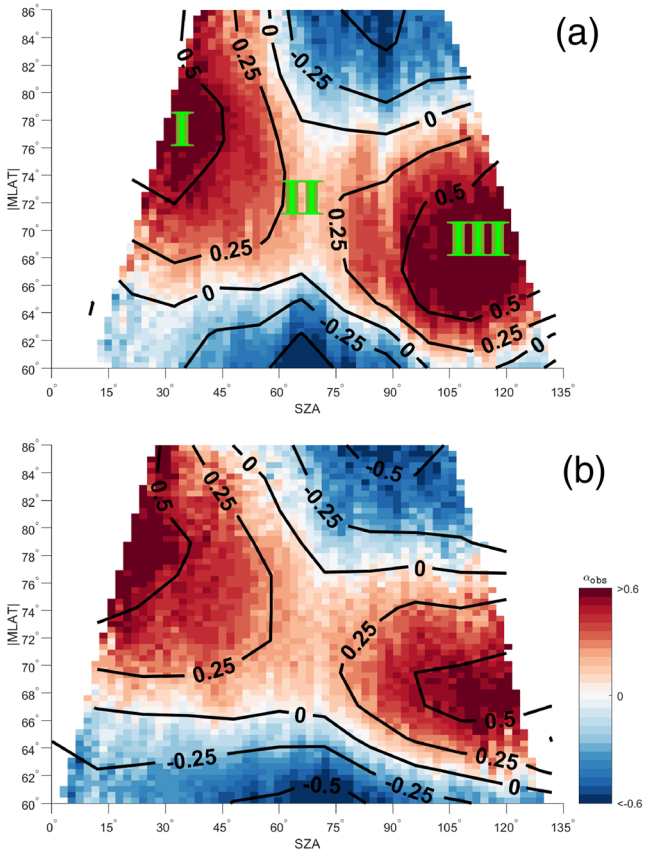

Figure 6. The distribution of α_{obs}, here binned by absolute MLAT (y axis) and SZA (x axis), in a 64 × 64 grid, for the Northern (a) and Southern (b) Hemispheres. Also shown are contour lines of constant α_{obs} (calculated on a 12 × 12 grid) as a visual aid. Three regimes are marked in green roman numerals; high MLAT-low SZA (I), intermediate MLAT-intermediate SZA (II), and low MLAT-high SZA (III). The data used come from Swarm A, span a time period from 18 January 2014 until 3 March 2019, and consist of 9.9 million 6 s segments from the Northern Hemisphere and 7.5 million from the Southern Hemisphere. Bins in MLAT-SZA with bin populations of less than 100 were discarded.

each year. Panels (a), (c), and (e) contain Northern Hemisphere data, while Panels (b), (d), and (f) contain Southern Hemisphere data.

For all seasons, the distribution of highly positive α_{obs} is co-located with the well-known distribution of diffuse aurora, both on the dayside and the nightside (Han et al., 2015; Newell et al., 2010). Clear seasonal dependencies in the distribution of α_{obs} are visible. For both hemispheres, α_{obs} peaks on the nightside during local winter, roughly between 64° and 72° MLAT. In the Northern Hemisphere, $\alpha_{obs} > 0.5$ throughout the nightside, while the values of α_{obs} are somewhat lower for the Southern Hemisphere. On the dayside, α_{obs} peaks during local summer, between 73° and 82° MLAT, for both hemispheres.

In Figure 5, we show the climatological distribution of the Poynting flux S_z (Equation 5), for the Northern (Panels a, b) and Southern (Panels c, d) Hemispheres. Panels (a) and (c) show downward going flux, while Panels (b) and (d) show upward going flux. The Poynting flux does not exhibit strong seasonal dependencies, and so Figure 5 includes data from all seasons. For both hemispheres, we see that the downward going S_z is clearly stronger than upward going flux for both hemispheres, with the downward going flux magnitude peaking in the pre-noon sector. The distribution of measured S_z is in clear agreement with previously reported global distributions of field-parallel Poynting flux (Gary et al., 1995; Keiling et al., 2003), and with statistical studies documenting the detection of ultralow-frequency (ULF) waves, in the Pc1-5 pulsation frequency ranges (Baddeley et al., 2004; Kim et al., 2011), intervals often associated with Alfvén waves.

To better discern the effect of SZA, and thus of underlying ionospheric Pedersen conductance on the Alfvén wave reflection climatology, we present in Figure 6 α_{obs} binned by SZA (x axis) and absolute MLAT (y axis), in a 64 × 64 grid for the Northern (a) and Southern (b) Hemispheres. Here, we include all the data that adheres to the selection criteria detailed above, excluding individual bins the populations of which number less than 100. We provide contour lines of constant α_{obs} (calculated on a lower-resolution grid). For the Northern Hemisphere, three regimes are marked in green Roman Numerals I (high MLAT, low SZA), II (intermediate MLAT, intermediate SZA), and III (low MLAT, high SZA). Two clear regions of enhanced α_{obs} are situated at I (the *dayside* α_{obs} enhancements

seen in Figure 4) and III (the *nightside* α_{obs} enhancements seen in Figure 4). An intermediary regime of $\alpha_{obs} = 0$ is situated at II. The same pattern is valid for the Southern Hemisphere (Panel b).

4. Discussion

The seasonal dependencies visible in the distribution of α_{obs} (Figure 4) match the reported seasonal dependencies of the diffuse aurora, both on the dayside and the nightside (Liou et al., 2001; Newell et al., 2010; Nishimura et al., 2020) and, in particular, the general distribution of pulsating aurora (Grono & Donovan, 2020). For the most part, we do not observe an enhancement of α_{obs} co-located with monoenergetic or broadband aurora, which primarily are distributed poleward of ±70° MLAT in the evening sector (Newell et al., 2009) and carries a wide range of electron energies (Fang et al., 2010). We thus observe a strong co-location between the high-energy deeply penetrating electron precipitation of the diffuse aurora and increases in α_{obs}. However, the relationship between diffuse aurora-induced Hall conductance and enhanced values of Alfvén wave reflection, which we will now explore, goes deeper than a mere co-location. Consider the regimes marked by roman numerals in Figure 6a. The regime labeled with Roman Numeral I is characterized by high MLAT and low SZA, which coincides with the summer hemisphere daytime cusp. This region sees soft precipitation directly from the magnetosheath. Despite the very high-number flux, the daytime precipitation does not carry high-energy deeply penetrating electrons and so will have a limited impact on Hall conductance (Kwak & Richmond, 2007; Liou et al., 2001; Vickrey et al., 1981). This low-energy high-number flux precipitation will, however, have a high impact on Pedersen conductance (Coumans et al., 2004; Vickrey et al., 1981). In addition, the comparatively low values of SZA in this region lead both Pedersen and Hall conductances to receive moderate contributions from EUV photoionization (Brekke & Moen, 1993; Ridley et al., 2004). Due to the low-energy dayside auroral precipitation, Regime I can then be considered a relatively high-Σ_P low-Σ_H regime, and the observed increase in α_{obs} is wholly expected and predicted by the classical α_0 (Equation 1). Conversely, Regime II is characterized by a moderately high SZA and is situated away from the ion outflow of the cusp. Without any predicted enhancement of Pedersen conductance, we then expect no increase in α_{obs} here. In Figure 6a, this region exhibits average values of $\alpha_{obs} \approx 0$. Regimes I and II in Figure 6a can then be explained by the corresponding Regimes I and II in the illustrating Figure 2.

The strongly enhanced α_{obs} in the regime marked by Roman Numeral III (Figure 6a), on the other hand, cannot be explained using the classical Alfvén reflection coefficient. This region is characterized by lower MLAT (roughly between 64° and 73°), and very high SZA (>100°). Due to complete lack of EUV photoionization in this regime, Pedersen conductance should be low (Moen & Brekke, 1993; Vickrey et al., 1981). Based on Equation 1, then, this region should not exhibit enhanced values of α_{obs}, since the Alfvén conductance in Equation 1 does not vary strongly with SZA. However, this regime is dominated by the nightside diffuse aurora, which provides high-energy deeply penetrating electrons (Newell et al., 2010; Nishimura et al., 2020). In addition, since SZA > 90°, Regime III contains data points sampled exclusively in darkness, when precipitating electrons tend to carry higher energy (Liou et al., 2001). (Note that Regime III does not contain data from the cusp region.)

Deeply penetrating electron precipitation in Regime III will strongly impact Hall conductance (Coumans et al., 2004; Vickrey et al., 1981). Indeed, Senior et al. (1982) and Hosokawa et al. (2010) measured ratios of $\Sigma_H/\Sigma_P \approx 3$ under the diffuse aurora. Regime III can then be considered a high-Σ_H regime. According to the model presented in Yoshikawa and Itonaga (2000), this increase in Hall conductance should increase α_{obs} substantially (Yoshikawa & Itonaga, 2000). As illustrated by the dot-dashed line in Figure 2, an increase in the energy of precipitating electrons from 0.5 to 8 keV has the capacity, under the example conditions of Figure 2, to raise α from 0 to 0.6, corresponding to a transition from II to III. We observe a clear enhancement in α_{obs} in Regime III, which we interpret as evidence for the role of Hall conductance in the Alfvén wave reflection climatology.

The early morning sector, where we to a large degree observe the low-Σ_P high-Σ_H regime, is not characterized by a particularly strong Poynting flux (Figure 5). However, the highly positive Alfvén wave reflection coefficient here yields an increase in local FAC through positive wave interference. This increase in FAC comes in addition to electron precipitation in the diffuse aurora, highlighting the duality between electromagnetic energy flux and auroral precipitation in the magnetosphere-ionosphere energy transfer, and should be seen in context with reports that electromagnetic Poynting flux powers auroral precipitation (Keiling et al., 2003, 2020). Furthermore, the co-location of areas of enhanced α_{obs} and of pulsating aurora

(Grono & Donovan, 2020) should likewise be seen in context with reports that pulsating aurora significantly modulates the FAC system (Hosokawa et al., 2010).

Recently, Workayehu et al. (2020), found that auroral currents (both FACs and *E* region horizontal currents) are stronger in the Northern Hemisphere compared to the Southern Hemisphere, an asymmetry that cannot be explained by a different hemispheral distribution in SZA. Additionally, the authors report, this asymmetry is stronger between local winter seasons. This, then, can be explained by the hemispheral asymmetry visible we find in Figure 4, where α_{obs}, and hence also precipitation-induced conductance, is stronger in the Northern Hemisphere compared to the Southern Hemisphere, and especially so in the case of local winter season (Panels e and f). Finally, regarding the high-latitude distribution of Poynting flux (Figure 5), it is important to bear in mind the following. The high-pass filter applied to the raw *E* field data, which is intended to correct for large-scale offsets, does to a certain degree suppress the Poynting flux magnitude, causing the flux displayed in Figure 5 to be somewhat lower than previous investigations have shown. The results presented in the present study are, however, qualitatively consistent both with or without filtering the raw *E* field data.

5. Conclusion

In this study, we present a large statistical analysis of Alfvén wave reflection based on in situ satellite observations from the Swarm mission for both the Northern and Southern Hemispheres. We have discovered three distinct regimes in the Alfvén climatology, two of which can be explained by classical Alfvén wave reflection and one which cannot. The latter regime, characterized by a relatively low Pedersen conductance and a high Hall conductance, is explained by the theoretical work presented by Yoshikawa and Itonaga (2000). This greatly increased role of Hall conductance has been pointed out in the theoretical literature but has hitherto not been observed in situ. Our results provide observational evidence for this new role of Hall conductance in the ionospheric wave reflection climatology.

However, further investigations into the link between Hall conductance and Alfvén wave reflection are needed, for example by application of numerical models. We hope the result presented in the present study might encourage future investigations into the matter.

Data Availability Statement

The Thermal Ion Imager data set can be accessed online (through https://earth.esa.int/web/guest/swarm/data-access).

Acknowledgments
The authors acknowledge the University of Calgary EFI team for the Thermal Ion Imager data set. The data set is covered by "EFI TII Cross-Track Flow Data Release Notes," Doc. no: SW-RN-UoC-GS-004, Rev: 4, 5 February 2020. Swarm is a European Space Agency mission with significant support from the Canadian Space Agency for the EFI data calibration and processing. J. P. and Y. S. K. were supported by the Air Force Office of Scientific Research (AFOSR) grant FA2386-18-1-0107. The authors are grateful to J. Wu and J. Burchill for discussions, and to I. Ivarsen for proofreading.

References

Alfvén, H. (1942). Existence of electromagnetic-hydrodynamic waves. *Nature*, *150*(3805), 405–406. https://doi.org/10.1038/150405d0

Baddeley, L. J., Yeoman, T. K., Wright, D. M., Trattner, K. J., & Kellet, B. J. (2004). A statistical study of unstable particle populations in the global ringcurrent and their relation to the generation of high m ULF waves. *Annales Geophysicae*, *22*(12), 4229–4241. Retrieved 2020-08-06, from https://hal.archives-ouvertes.fr/hal-00317788. Publisher: European Geosciences Union.

Brekke, A., & Moen, J. (1993). Observations of high latitude ionospheric conductances. *Journal of Atmospheric and Terrestrial Physics*, *55*(11), 1493–1512. https://doi.org/10.1016/0021-9169(93)90126-J

Burke, W. J., Martinis, C. R., Lai, P. C., Gentile, L. C., Sullivan, C., & Pfaff, R. F. (2016). C/NOFS observations of electromagnetic coupling between magnetically conjugate MSTID structures. *Journal of Geophysical Research: Space Physics*, *121*, 2569–2582. https://doi.org/10.1002/2015JA021965

Coumans, V., Gérard, J. C., Hubert, B., Meurant, M., & Mende, S. B. (2004). Global auroral conductance distribution due to electron and proton precipitation from IMAGE-FUV observations. *Annales Geophysicae*, *22*(5), 1595–1611. https://doi.org/10.5194/angeo-22-1595-2004

Cowley, S. W. H. (2000). TUTORIAL: Magnetosphere-ionosphere interactions: A tutorial review. *Washington DC American Geophysical Union Geophysical Monograph Series*, *118*, 91. https://doi.org/10.1029/GM118p0091

Cowley, S. W. H., & Lockwood, M. (1992). Excitation and decay of solar wind-driven flows in the magnetosphere-ionosphere system. *Annales Geophysicae*, *10*, 103–115. Retrieved 2018-03-07, from http://adsabs.harvard.edu/abs/1992AnGeo..10..103C

Coxon, J. C., Milan, S. E., Carter, J. A., Clausen, L. B. N., Anderson, B. J., & Korth, H. (2016). Seasonal and diurnal variations in AMPERE observations of the Birkeland currents compared to modeled results. *Journal of Geophysical Research: Space Physics*, *121*, 4027–4040. https://doi.org/10.1002/2015JA022050

Dungey, J. W. (1961). Interplanetary magnetic field and the auroral zones. *Physical Review Letters*, *6*, 47–48. https://doi.org/10.1103/PhysRevLett.6.47

Fang, X., Randall, C. E., Lummerzheim, D., Wang, W., Lu, G., Solomon, S. C., & Frahm, R. A. (2010). Parameterization of monoenergetic electron impact ionization. *Geophysical Research Letters*, *37*, L22106. https://doi.org/10.1029/2010GL045406 (Publisher: John Wiley & Sons, Ltd.)

Fedorov, E., Mazur, N., Pilipenko, V., & Engebretson, M. (2016). Interaction of magnetospheric Alfvén waves with the ionosphere in the Pc1 frequency band. *Journal of Geophysical Research: Space Physics*, *121*, 321–337. https://doi.org/10.1002/2015JA021020

Fedorov, E. N., Pilipenko, V. A., Engebretson, M. J., & Hartinger, M. D. (2018). Transmission of a magnetospheric Pc1 wave beam through the ionosphere to the ground. *Journal of Geophysical Research: Space Physics*, *123*, 3965–3982. https://doi.org/10.1029/2018JA025338

Friis-Christensen, E., Lühr, H., & Hulot, G. (2006). Swarm: A constellation to study the Earth's magnetic field. *Earth, Planets and Space*, *58*, BF03351933. https://doi.org/10.1186/BF03351933

Fujii, R., Iijima, T., Potemra, T. A., & Sugiura, M. (1981). Seasonal dependence of large-scale Birkeland currents. *Geophysical Research Letters*, *8*(10), 1103–1106. https://doi.org/10.1029/GL008i010p01103

Gary, J. B., Heelis, R. A., & Thayer, J. P. (1995). Summary of field-aligned Poynting flux observations from DE 2. *Geophysical Research Letters*, *22*(14), 1861–1864. https://doi.org/10.1029/95GL00570

Grono, E., & Donovan, E. (2020). Surveying pulsating auroras. *Annales Geophysicae*, *38*(1), 1–8. (Publisher: Copernicus GmbH). https://doi.org/10.5194/angeo-38-1-2020

Han, D. S., Chen, X. C., Liu, J. J., Qiu, Q., Keika, K., Hu, Z. J., & Yang, H. G. (2015). An extensive survey of dayside diffuse aurora based on optical observations at Yellow River Station. *Journal of Geophysical Research: Space Physics*, *120*, 7447–7465. https://doi.org/10.1002/2015JA021699

Haraguchi, K., Kawano, H., Yumoto, K., Ohtani, S., Higuchi, T., & Ueno, G. (2004). Ionospheric conductivity dependence of dayside region-0, 1, and 2 field-aligned current systems: Statistical study with DMSP-F7. *Annales Geophysicae*, *22*(8), 2775–2783. https://doi.org/10.5194/angeo-22-2775-2004

Hosokawa, K., Ogawa, Y., Kadokura, A., Miyaoka, H., & Sato, N. (2010). Modulation of ionospheric conductance and electric field associated with pulsating aurora. *Journal of Geophysical Research*, *115*, A03201. https://doi.org/10.1029/2009JA014683

Iijima, T., & Potemra, T. A. (1978). Large-scale characteristics of field-aligned currents associated with substorms. *Journal of Geophysical Research*, *83*(A2), 99–615. https://doi.org/10.1029/JA083iA02p00599

Keiling, A., Thaller, S., Dombeck, J., & Wygant, J. (2020). Temporal evolution of substorm-driven global Alfvén wave power above the auroral acceleration region. *Journal of Geophysical Research: Space Physics*, *125*, e2019JA027444. https://doi.org/10.1029/2019JA027444

Keiling, A., Wygant, J. R., Cattell, C. A., Mozer, F. S., & Russell, C. T. (2003). The global morphology of wave Poynting flux: Powering the aurora. *Science*, *299*(5605), 383–386. https://doi.org/10.1126/science.1080073 Publisher: American Association for the Advancement of Science Section: Report.

Kim, H., Lessard, M. R., Engebretson, M. J., & Young, M. A. (2011). Statistical study of Pc1–2 wave propagation characteristics in the high-latitude ionospheric waveguide. *Journal of Geophysical Research*, *116*, A07227. https://doi.org/10.1029/2010JA016355

Knudsen, D. J. (1990). Alfvén waves and static fields in magnetosphere/ionosphere coupling: In-situ measurements and a numerical model (Doctoral dissertation). Retrieved 2020-08-10, from https://adsabs.harvard.edu/abs/1990PhDT.....35K (Journal Abbreviation: PhD thesis Publication Title: PhD thesis).

Knudsen, D. J., Burchill, J. K., Buchert, S. C., Eriksson, A. I., Gill, R., Wahlund, J. E., & Moffat, B. (2017). Thermal ion imagers and Langmuir probes in the Swarm electric field instruments. *Journal of Geophysical Research: Space Physics*, *122*, 2655–2673. https://doi.org/10.1002/2016JA022571

Kwak, Y. S., & Richmond, A. D. (2007). An analysis of the momentum forcing in the high-latitude lower thermosphere. *Journal of Geophysical Research*, *112*, A01306. https://doi.org/10.1029/2006JA011910

Liou, K., Newell, P. T., & Meng, C. I. (2001). Seasonal effects on auroral particle acceleration and precipitation. *Journal of Geophysical Research*, *106*(A4), 5531–5542. https://doi.org/10.1029/1999JA000391

Lomidze, L., Burchill, J. K., Knudsen, D. J., Kouznetsov, A., & Weimer, D. R. (2019). Validity study of the Swarm horizontal cross-track ion drift velocities in the high-latitude ionosphere. *Earth and Space Science*, *6*(3), 411–432. https://doi.org/10.1029/2018EA000546

Lotko, W., Smith, R. H., Zhang, B., Ouellette, J. E., Brambles, O. J., & Lyon, J. G. (2014). Ionospheric control of magnetotail reconnection. *Science*, *345*(6193), 184–187. Publisher: American Association for the Advancement of ScienceSection: Report. https://doi.org/10.1126/science.1252907

Lysak, R. L. (1991). Feedback instability of the ionospheric resonant cavity. https://doi.org/10.1029/90JA02154

Moen, J., & Brekke, A. (1993). The solar flux influence on quiet time conductances in the auroral ionosphere. *Geophysical Research Letters*, *20*(10), 971–974. https://doi.org/10.1029/92GL02109

Newell, P. T., Sotirelis, T., & Wing, S. (2009). Diffuse, monoenergetic, and broadband aurora: The global precipitation budget. *Journal of Geophysical Research*, *114*, A09207. https://doi.org/10.1029/2009JA014326

Newell, P. T., Sotirelis, T., & Wing, S. (2010). Seasonal variations in diffuse, monoenergetic, and broadband aurora. *Journal of Geophysical Research: Space Physics*, *115*, A03216. https://doi.org/10.1029/2009JA014805

Nishimura, Y., Lessard, M. R., Katoh, Y., Miyoshi, Y., Grono, E., Partamies, N., & Kurita, S. (2020). Diffuse and pulsating aurora. *Space Science Reviews*, *216*(1), 4. https://doi.org/10.1007/s11214-019-0629-3

Pakhotin, I. P., Mann, I. R., Lysak, R. L., Knudsen, D. J., Gjerloev, J. W., Rae, I. J., & Balasis, G. (2018). Diagnosing the role of Alfvén waves in magnetosphere-ionosphere coupling: Swarm observations of large amplitude nonstationary magnetic perturbations during an interval of northward IMF. *Journal of Geophysical Research: Space Physics*, *123*, 326–340. https://doi.org/10.1002/2017JA024713

Park, J., Lühr, H., Knudsen, D. J., Burchill, J. K., & Kwak, Y. S. (2017). Alfvén waves in the auroral region, their Poynting flux, and reflection coefficient as estimated from Swarm observations. *Journal of Geophysical Research: Space Physics*, *122*, 2345–2360. https://doi.org/10.1002/2016JA023527

Ridley, A. J., Gombosi, T. I., & DeZeeuw, D. L. (2004). Ionospheric control of the magnetosphere: Conductance. *Annales Geophysicae*, *22*(2), 567–584. https://doi.org/10.5194/angeo-22-567-2004

Senior, C., Robinson, R. M., & Potemra, T. A. (1982). Relationship between field-aligned currents, diffuse auroral precipitation and the westward electrojet in the early morning sector. *Journal of Geophysical Research*, *87*(A12), 10,469–10,477. https://doi.org/10.1029/JA087iA12p10469

Siscoe, G. L. (1983). Solar system magnetohydrodynamics, *Solar-terrestrial physics* (pp. 11–100). Dordrecht: Springer Netherlands. https://doi.org/10.1007/978-94-009-7194-3_2

Siscoe, G. L., & Huang, T. S. (1985). Polar cap inflation and deflation. *Journal of Geophysical Research*, *90*(A1), 543–547. https://doi.org/10.1029/JA090iA01p00543

Vickrey, J. F., Vondrak, R. R., & Matthews, S. J. (1981). The diurnal and latitudinal variation of auroral zone ionospheric conductivity. *Journal of Geophysical Research*, *86*(A1), 65–75. https://doi.org/10.1029/JA086iA01p00065

Waters, C. L., Anderson, B. J., Greenwald, R. A., Barnes, R. J., & Ruohoniemi, J. M. (2004). High-latitude poynting flux from combined Iridium and SuperDARN data. *Annales Geophysicae*, *22*(8), 2861–2875. https://doi.org/10.5194/angeo-22-2861-2004 Publisher: Copernicus GmbH.

Waters, C. L., Lysak, R. L., & Sciffer, M. D. (2013). On the coupling of fast and shear Alfvén wave modes by the ionospheric Hall conductance. *Earth, Planets and Space*, *65*(5), 2. https://doi.org/10.5047/eps.2012.08.002

Workayehu, A. B., Vanhamäki, H., & Aikio, A. T. (2020). Seasonal effect on hemispheric asymmetry in ionospheric horizontal and field-aligned currents. *Journal of Geophysical Research: Space Physics*, *125*, e2020JA028051. https://doi.org/10.1029/2020JA028051

Yamamoto, T., Ozaki, M., & Inoue, S. (2003). Relationship between ionospheric conductivity and intensity of the daytime region 1 field-aligned current in geomagnetically quiet conditions. *Journal of Geophysical Research*, *108*(A5), 1190. https://doi.org/10.1029/2002JA009607

Yoshikawa, A., & Itonaga, M. (1996). Reflection of shear Alfvén waves at the ionosphere and the divergent Hall current. *Geophysical Research Letters*, *23*(1), 101–104. https://doi.org/10.1029/95GL03580

Yoshikawa, A., & Itonaga, M. (2000). The nature of reflection and mode conversion of MHD waves in the inductive ionosphere: Multistep mode conversion between divergent and rotational electric fields. *Journal of Geophysical Research*, *105*(A5), 10,565–10,584. https://doi.org/10.1029/1999JA000159